Phonon dispersion anomalies and superconductivity in metal substituted MgB_2

Ian D.R. Mackinnon *, Peter C. Talbot, Jose A. Alarco

Institute for Future Environments and Science and Engineering Faculty, QUT 2 George Street, Brisbane, QLD 4001, Australia

ABSTRACT

We have calculated the extent of the E_{2g} phonon anomaly for $Mg_{1-x}M_xB_2$ where M = Sc, Ti, Cd and Ba for $0 < x < 1$ using *ab initio* DFT models with the LDA and GGA functionals. Using superlattice models along the *c* axis to represent metal substitution in MgB_2, we show that phonon dispersion (PD) plots vary significantly with x, in particular, the nature and extent of the phonon anomaly around the origin, **G**, of the reciprocal lattice. Measurement of this phonon anomaly along the **G-K** and **G-M** directions provides an estimate of the thermal energy, T_δ, of the anomaly, which approximates experimentally determined T_c within standard error for Sc and Ti substitution. We demonstrate that substitutions of Cd and Ba in MgB_2 show a higher calculated T_δ than MgB_2 by more than 20 K. Syntheses of these Cd and Ba compositions are not extant and may not be possible given the limited solubility of metals in MgB_2. Nevertheless, *ab initio* DFT models of phonon behaviour in AlB_2–type structures provide an effective tool for prediction of physical properties and for design of new materials.

© 2017 The Author(s). Published by Elsevier B.V. This is an open access article under the CC BY-NC-ND license (http://creativecommons.org/licenses/by-nc-nd/4.0/).

1. Introduction

A review of the metal boride and metal borocarbide literature [1], indicates that more than eighty stoichiometric compounds are superconductors. The simple diboride, MgB_2, shows a superconducting transition temperature, T_c, that is higher than all metal borides at 38.7 K [2] and is about twice as high as the highest T_c for binary superconductors (e.g. Nb_3Ge) [1]. A proportion (<20%) of the boride and borocarbide suite shows T_c values above 10 K but few show $T_c > 20$ K [1]. Despite many attempts [3–5] to increase the T_c of MgB_2 by inserting other elements into the structure [4], experiment shows that substitution of another metal for Mg invariably results in suppression of T_c [3].

The limited solubility of many metals in MgB_2 suggests it is very difficult to produce a substituted form of MgB_2 (i.e. $Mg_{1-x}M_xB_2$, where $0 < x < 1$) let alone one that shows a T_c higher than 39 K [2]–40 K [6]. A number of authors [3–5,7] show that three substituted forms – $Mg_{1-x}Al_xB_2$, $Mg_{1-x}Mn_xB_2$ and $Mg(B_{1-x}C_x)_2$ – are reliable and reproducible compositions for which T_c decreases with increasing substitution albeit *via* different mechanisms [6]. Two other substituted forms are $Mg_{1-x}Sc_xB_2$ [8–11] and $Mg_{1-x}Ti_xB_2$ [12] for which experimental data confirm the trend of a decrease

in T_c with increase in substituted metal. In this study, we evaluate the phonon behaviour of these compounds as well as other metal substituted forms that show contrary behaviour (e.g. Ba and Cd substitution).

Vibrations of boron atoms in the *a-b* plane, exemplified by the E_{2g} phonon modes, are shown by experiment [13,14] and theory [15,16] to be critical to understanding superconducting behaviour in MgB_2 and metal substituted forms [3,17]. Fig. 1 shows the structure of MgB_2 and of $Mg_{1-x}M_xB_2$, (for x = 0. 33) with P6/mmm symmetry and, along the *c*-axis direction, alternating layers of boron and metal atoms in hexagonal configuration. The E_{2g} phonon modes are ascribed to the motions of boron atoms within the *a-b* plane as shown and are readily detected using Raman spectroscopy [13,18] and inelastic X-ray scattering (IXS) [14,19,20]. The vibrations of atoms are also calculable *via* Density Functional Theory (DFT) which presents the collective excitations of atoms at a single frequency in a solid as phonons, and which by their nature, are temperature dependent.

The wave vectors and quantized energies of all atom vibrations are depicted in phonon dispersion (PD) plots which are described in greater detail in recent reviews [21,22]. In earlier work [18,23], we demonstrate that the presence or absence of a phonon anomaly, also known as a Kohn anomaly, particularly associated with the E_{2g} phonon modes either side of the reciprocal space origin, is indicative for AlB_2–type solids that behave (or not) as a superconductor. This analysis, based on *ab initio* DFT calculations,

* Corresponding author.
E-mail addresses: ian.mackinnon@qut.edu.au (I.D.R. Mackinnon), p.talbot@qut.edu.au (P.C. Talbot), jose.alarco@qut.edu.au (J.A. Alarco).
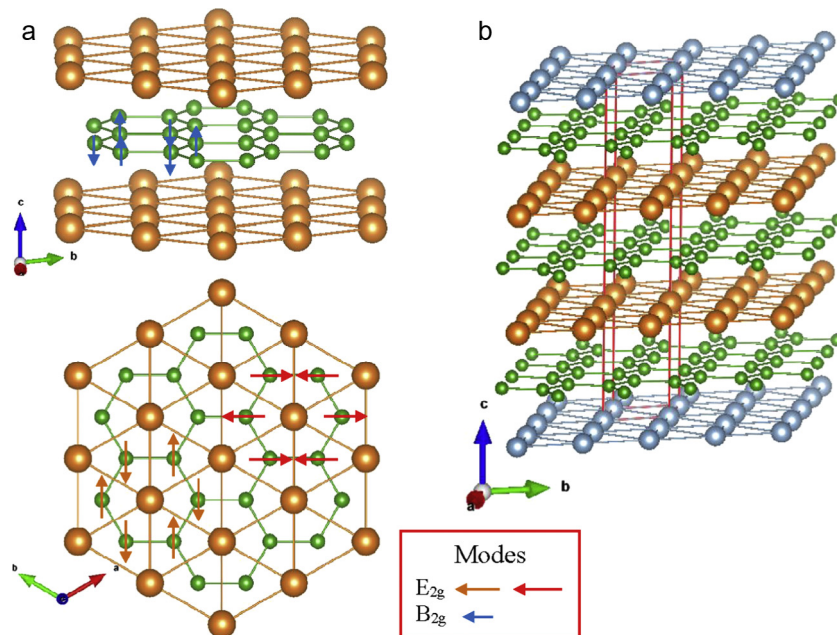
Fig. 1. Schematic of the AlB$_2$-type structure and relationship of key atom vibration modes to real space directions. (a) Alternating layers of Mg (gold spheres) and B (green spheres) for MgB$_2$ viewed at an angle to the a-axis direction and down the c-axis. (b) Schematic of an Mg$_2$MB$_6$ superlattice structure showing alternating layers of Mg, B and substituted metal, M. (For interpretation of the references to color in this figure legend, the reader is referred to the web version of this article.)

is robust for Al-substituted MgB$_2$ in that experimental T$_c$ values and calculated values for the thermal energy of the phonon anomaly are equivalent within systematic error [23]. For the case of Mg$_{1-x}$Al$_x$B$_2$, and disilicide AlB$_2$-type structures [23], the valence electrons at or near the Fermi level are in s and p orbitals. In this study, we examine the influence of d orbitals due to substitution of transition metals into the MgB$_2$ structure. In addition, we evaluate new, predicted compositions that may have superconducting properties and that may show, via experiment, transition temperatures higher than 40 K.

2. Computational methods

DFT calculations are undertaken using the CASTEP module of Materials Studio 8.0, which provides the functionality to calculate vibrational properties for a wide range of materials [24,25]. Both linear response (also known as density functional perturbation theory, DFPT) and finite displacement (FD) methods from this software suite are used. Calculation methods for optimum PD results on MgB$_2$ are reported earlier [18,26]. The linear response within the Local Density Approximation (LDA) and Generalized Gradient Approximation (GGA) with norm-conserving pseudo-potentials, a plane-wave basis set and a dense k–grid (predominantly at k $\leqslant$ 0.03 Å^{-1}) provide the most consistent model outcomes for a wide range of AlB$_2$-type compositions [18,23].

On advice from reviewers, we have also evaluated model calculations using DFT+U methods in order to include spin polarization for metals with d orbitals [27,28]. The electronic band structures and Fermi surfaces of several Sc-substituted cases have been calculated using both LDA+U and GGA + U methods. Our calculations for Sc-substituted MgB$_2$ using LDA+U results in almost identical electronic band structures and Fermi surfaces to those obtained using LDA and GGA. Calculations using GGA+U results in a small splitting of the alpha and beta spin-polarized components without significant changes to the major features of the electronic bands and Fermi surfaces. An example of these DFT+U calculations for Mg$_5$ScB$_{12}$ is provided in Supplemental Material (Fig. S1). We note that the shape of a phonon anomaly is largely determined by

nesting across Fermi surfaces [23], but these surfaces have not been significantly altered by calculations using DFT + U. Hence, we have not pursued DFT + U methods in any further depth for this study.

We have shown previously that the k-grid value is a critical parameter for interpretation of PD plots [18,23,26]. While all calculations for this structure type are not shown in this work, k-grid values ranging from 0.04 Å^{-1} to 0.015 Å^{-1} (in increments of 0.005 of the relative Brillouin zone length 0.5) have been evaluated. When PD calculations with these choices fail to converge, intermediate k-grid values are also evaluated. In the examples shown, we present DFT models with the smallest value of k-grid to achieve convergence. The values for the k-grid mesh density used in this work are comparable to, or higher than, that shown in earlier studies [13,16,18,29] that identified key changes in PD characteristics with this parameter. These potential changes to the PD include shifts in E$_{2g}$ frequency values at specific reciprocal lattice points [13,18,29] and the appearance of vibration mode branches in PD plots [18].

We use the High Performance Computing (HPC) facility at QUT using numbers of cores that are multiples of the k–grid in a and b reciprocal space directions [18]. The cut-off energy value $\sim$990 eV is as previously used for the Mg$_{1-x}$Al$_x$B$_2$ series [23]. Convergence criteria for most calculations are as follows: energy at 5×10^{-6} eV per atom; maximum force at 0.01 eV Å^{-1}; maximum stress at 0.02 GPa and maximum atom displacement at 5×10^{-4} Å. For end member compositions, optimized unit cell parameters are based on literature values for MgB$_2$, AlB$_2$, ScB$_2$, and TiB$_2$ [18,26,30–32]. Schematic models of crystal structures shown in Fig. 1 are built using optimized cell parameters from CASTEP as input to the program VESTA [33].

The current version of CASTEP incorporated into Materials Studio 8.0 does not adequately support utilization of the Virtual Crystal Approximation (VCA) formalism to calculate PDs for disordered or randomly substitutional models [34]. Furthermore, when we use fractional occupancy substitution (rather than doping), geometry optimization for AlB$_2$-type structures often results in a c-axis parameter that has a large deviation ($\sim$1 Å) from experimental. This phenomena appears unique to the CASTEP code which uses

full plane waves. Other programs, which use augmented plane waves, appear to incorporate fractional occupancy in a more facile manner [35]. Hence, in this work we utilize superlattice models along the *c*-axis of the AlB_2-type structure to evaluate intermediate compositions in $Mg_{1-x}Sc_xB_2$, $Mg_{1-x}Ti_xB_2$, $Mg_{1-x}Cd_xB_2$ and $Mg_{1-x}Ba_xB_2$. This computational strategy, presented in detail in earlier work [18,23], allows multiple integer constructs to represent substitution of the relevant metal atom with P6/mmm symmetry. For example, $MgScB_4$ modelled as a superlattice is equivalent to $(Mg_{0.5}Sc_{0.5})B_2$ while Mg_4ScB_{10} is equivalent to $(Mg_{0.8}Sc_{0.2})B_2$. An example of an ordered superlattice structure for Mg_2MB_6 is shown in Fig. 1b.

Superlattices are observed experimentally in Al-substituted MgB_2 along the *c*-axis direction and also in the *a-b* plane [3,17,36]. These latter superlattices are of ~10 nm dimension [36] and of minimal significance at unit cell scale to the dominant phenomena along the *c*-axis described in this work. For $Mg_{0.5}Al_{0.5}B_2$, an alternation of Al and Mg layers along the *c*-axis inherently results in a superlattice as observed by electron microscopy [3,37]. We show for the $Mg_{1-x}Al_xB_2$ series [23], that calculated enthalpies favor superlattice constructs with alternating layers of Mg and Al. In comparison, motifs that develop large segments of Mg–only or Al–only layers along the *c*-axis show less favorable enthalpy values [23]. These superlattice constructs assume infinitely periodic crystals of AlB_2–type material yet, in practice, these materials are likely to display domains with different stacking characteristics [36], particularly when differences in enthalpy are small. This computational method to model substituted MgB_2 is suited to the AlB_2-type structure but may not be an effective modeling strategy for all crystal structures.

3. Results

We provide details of PD calculations for metal-substituted MgB_2 compositional series that are based on, and related to, electronic band structure calculations [23] and are computed from the same DFT algorithms [24,25]. Electronic band structure and density of states (DOS) calculations for the end-member compositions calculated with k = 0.02 Å^{-1} using the LDA and GGA functionals are similar to DFT calculations obtained previously for MgB_2 [15,38], AlB_2 [39], ScB_2 [32,40] and TiB_2 [41–43]. As shown in earlier studies, the band structures for these end-member compositions are different in the **G–K** and **G–M** directions above and below the Fermi level. In particular, the complexity of band struc-

ture for ScB_2 is significantly increased compared with MgB_2 and the influence of d orbital character is evident in the DOS plot [32,40]. For ScB_2, the density of electrons (per eV) at the Fermi surface is ~2 times that of MgB_2 and AlB_2.
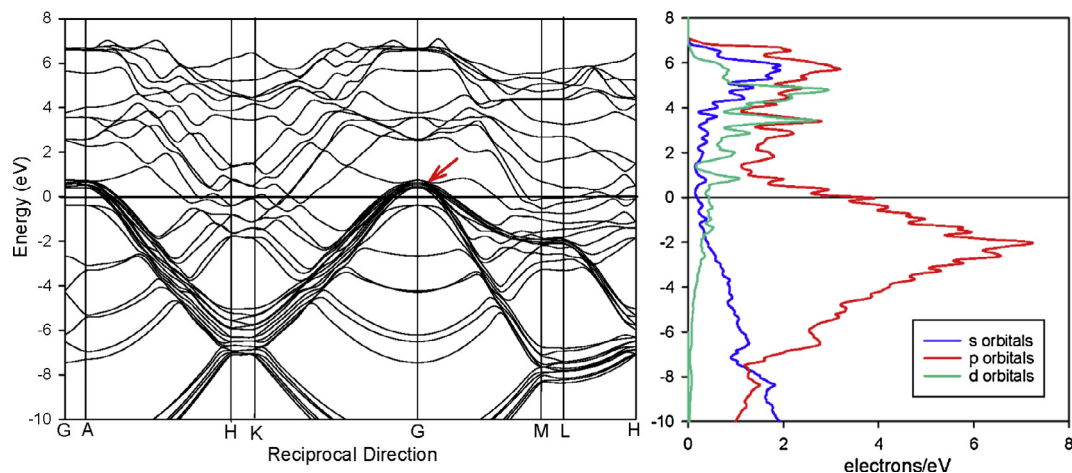
3.1. Band structure and density of states – $Mg_{1-x}Sc_xB_2$

For $Mg_{1-x}Sc_xB_2$, the influence of d orbitals on the calculated DOS at the vicinity of the Fermi level is evident with low amounts of substitution and the influence increases with increasing Sc content. Fig. 2 shows the band structure and DOS for Mg_5ScB_{12}, calculated using the LDA approximation with a k–grid of 0.016 Å^{-1} of the reciprocal space vector. The σ electronic bands of the superlattice appear as a bundle, indicating that a number of similarly behaved B planes in the superlattice multiply the σ band DOS. Despite a high Mg content, metal contributions to the Fermi level show significant d orbital character arising from Sc.

This d character influences phonons where electronic transitions between different sections of the Fermi Surface (FS) and its vicinity are prevalent as in MgB_2 [23]. The influence of Sc on the band structure is also shown in Supplemental Material (Fig. S2) for which the partial DOS (pDOS) for Mg and Sc are compared for compositions Mg_5ScB_{12} and Mg_2ScB_6. As the Sc content increases in $Mg_{1-x}Sc_xB_2$, the d orbitals and the s and p for both the Mg and Sc pDOS shift to higher energy.

3.2. Phonon dispersions

A PD plot for MgB_2 across all reciprocal lattice directions calculated using *ab initio* DFT with the GGA functional for k = 0.02 Å^{-1} is shown in Fig. 3. The anomaly reflected in the E_{2g} phonon mode(s) and centered on the reciprocal lattice origin, **G**, is highlighted by the green rectangle in Fig. 3. In the vicinity of the G-point, the E_{2g} PD bands are degenerate and extend along the basal plane directions (i.e., **G–K** and **G–M**) with a characteristic inflection along these directions that is limited, or defined, by the B_{2g} mode. This anomaly for MgB_2 is evident in other publications [18,23,26,44] when there is sufficient resolution of the k-grid and is referred to as a Kohn anomaly in earlier work [14,19,31]. The depth of this anomaly, δ, provides a measure of the thermal energy of the phonon anomaly for this structure type [23]. An alternative way to consider the anomaly, δ, is as the energy required for phonons at the lower energy region of the E_{2g} mode near the gamma point, **G**, to be excited to the B_{2g} mode. For this study, we will focus on

Fig. 2. *Ab initio* DFT band structure calculated for Mg_5ScB_{12} with the LDA functional and k = 0.016 Å^{-1}. The density of states section (right hand side) shows the contributions of s (blue), p (red) and d (green) orbitals at the FS. The critical σ bands at the cusp just above the FS are arrowed. (For interpretation of the references to color in this figure legend, the reader is referred to the web version of this article.)
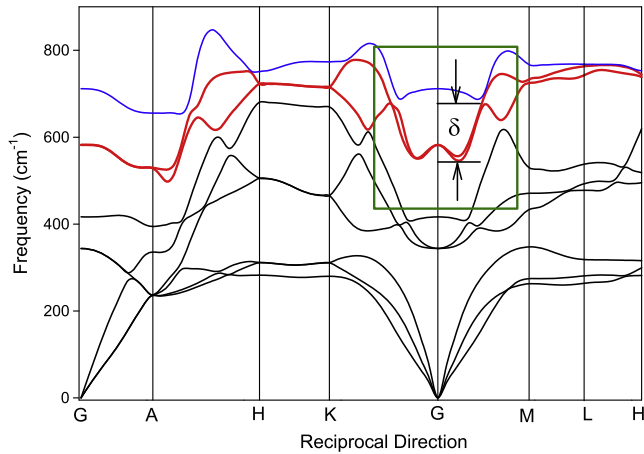
Fig. 3. Phonon dispersion (PD) plot for the MgB_2 structure that shows the frequencies of vibration with principal reciprocal lattice direction. The principal direction denoted **G** is at the origin of the reciprocal unit cell (i.e. [0,0,0]). Phonon branches that contain the E_{2g} phonon modes are highlighted in red; the B_{2g} mode is in dark blue. The green rectangle along the **G** direction is the location of the phonon (or Kohn) anomaly which varies in extent and form with metal substitution in MgB_2. (For interpretation of the references to color in this figure legend, the reader is referred to the web version of this article.)

partial PD plots for the reciprocal directions between **G-K** and **G-M,** which approximate the [100] and [110] real space directions in AlB_2-type structures.

Partial PD plots for four end-member compositions, MgB_2, AlB_2, ScB_2 and TiB_2, calculated using the LDA functional at k = 0.02 Å^{-1}

are shown in Fig. 4. In each case, the shape, frequency and relative order of the E_{2g} mode(s) at the G-point vary considerably. The phonon anomaly is clearly present in MgB_2 (Fig. 4a) and absent in AlB_2 (Fig. 4b) and TiB_2 (Fig 4d) consistent with experimental data on the presence and absence, respectively, of superconductivity in these compounds [45]. While a specific measurement of T_c for TiB_2 is not readily sourced in the literature, experimental data [46] and computational models [41,46] indicate that electron-phonon coupling is negligible. The partial PD for ScB_2 at **G** suggests a small anomaly is present in this structure.

The inclusion of d orbitals in DFT models of AlB_2-type structures not only increases computational demand but also adds a layer of complexity to interpretation. In Fig. 5, there are differences in the mode order and the shape of the PDs at optical phonon frequencies (i.e. $\omega > 450$ cm^{-1}) for Mg_2AlB_6 (Fig. 5a) and Mg_2ScB_6 (Fig. 5b). In Fig. 5a, the presence of a phonon anomaly at $\sim$600 cm^{-1} around **G** is evident for Mg_2AlB_6. The anomaly is less evident for Mg_2ScB_6 but is still suggestive of an inflection or change in reciprocal space direction around **G**. As shown in Fig. 5b, δ for x = 0.33 is smaller, and occurs at higher frequency, than that for Mg_2AlB_6. For Mg_2ScB_6, and similar compositions for which the phonon anomaly is small [23], the shape of the high frequency E_{2g} modes flattens or becomes less concave at, and in close proximity to, **G**. Similar behaviour of the E_{2g} mode for x = 0.4 in $Mg_{1-x}Al_xB_2$ is observed experimentally near **G** using very high resolution IXS [20].

Variations in mode shape and order are also evident with change in k-grid value for metal substitutions in MgB_2 that involve d orbitals. Fig. 6 shows the partial PD for $Mg_{0.83}Sc_{0.17}B_2$ and $Mg_{0.8}Sc_{0.2}B_2$ calculated using the LDA functional for k = 0.016 Å^{-1}. The superlattice models for these compositions are equivalent to
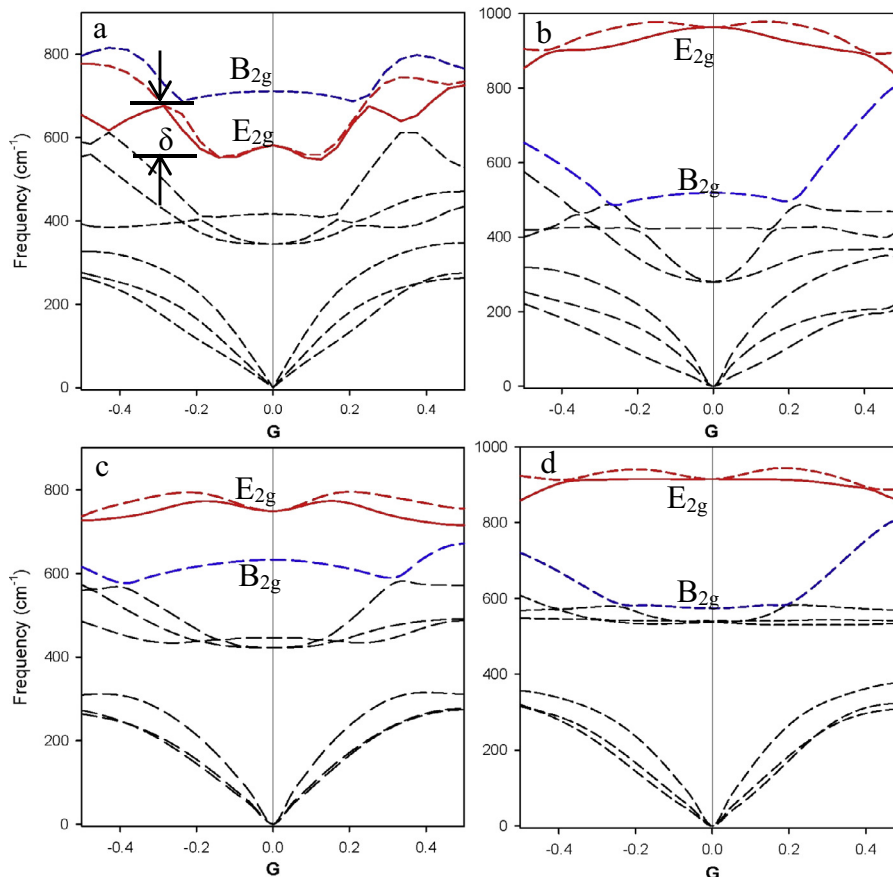
Fig. 4. Partial PD plots along the **G-K** and **G-M** directions for end-member compositions using *ab initio* DFT with the GGA functional for (a) MgB_2, (b) AlB_2, (c) ScB_2 and with the LDA functional for (d) TiB_2. Key optical phonon modes for each composition are identified. Note the asymmetric nature and higher frequency E_{2g} modes for AlB_2 and TiB_2.
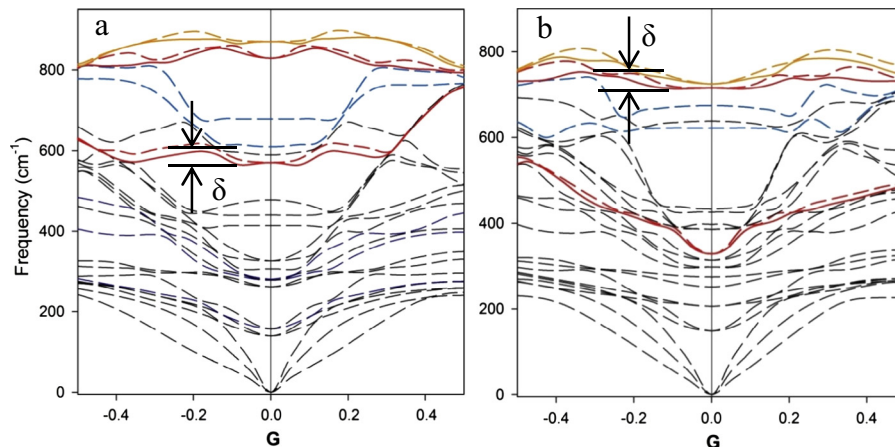
Fig. 5. Partial PD plots calculated using the GGA functional for (a) Mg_2AlB_6 at k = 0.02 Å^{-1} and (b) Mg_2ScB_6 at k = 0.017 Å^{-1}. E_{2g} phonon modes are highlighted in red, E_{2u} modes are orange and B_{2g} modes are blue. (For interpretation of the references to color in this figure legend, the reader is referred to the web version of this article.)
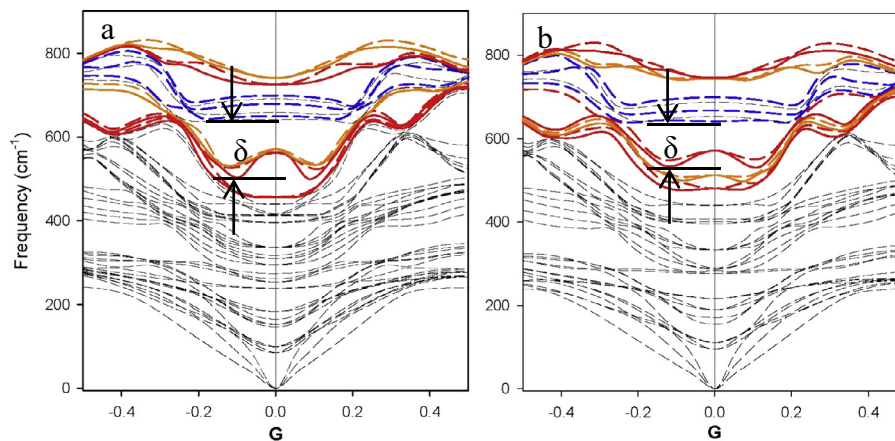
Fig. 6. Partial PD plots along the **G-M** and **G-K** reciprocal directions calculated using the LDA functional at k = 0.016 Å^{-1} for (a) Mg_5ScB_{12} and (b) Mg_4ScB_{10}. The E_{2g} phonon modes are highlighted in red, the E_{2u} modes are orange, the B_{2g} modes are dark blue and B_{1u} modes are light blue. Note that the difference in extent of the phonon anomaly, δ, is evident for a ∼3% difference in modelled Sc content. (For interpretation of the references to color in this figure legend, the reader is referred to the web version of this article.)

Mg_5ScB_{12} and Mg_4ScB_{10} or ordered multiples of 6× and 5× the basic MgB_2 unit cell. With increased Sc substitution, in this case a change of only 3%, a decrease in the extent of the phonon anomaly is observed and measured as shown in Table 1. Fig. 7 shows partial PD plots for $Mg_{0.5}Ti_{0.5}B_2$, $Mg_{0.75}Ti_{0.25}B_2$, $Mg_{0.66}Ba_{0.33}B_2$ and $Mg_{0.5}Cd_{0.5}B_2$ calculated by *ab initio* DFT using the GGA functionals for k ⩽ 0.02 Å^{-1}. The presence and extent of a phonon anomaly clearly varies with composition within a series and with different metal substituents.

3.3. Phonon anomaly thermal energy

Table 1 summarizes parameters determined by DFT calculations for selected compositions in the $Mg_{1-x}Sc_xB_2$ series. The examples shown in Table 1 represent optimized calculations based on evaluation of a much broader range of k–grid values as well as ordered and disordered compositions. As shown for the $Mg_{1-x}Al_xB_2$ series [23], these variables are first order determinants of computational convergence and consistency.

The calculated thermal energy, T_δ, associated with the presence of a phonon anomaly for a specific composition is listed in Table 1. The thermal energy, T_δ, for each composition is based on the equation:

$$\delta = \left(\frac{nN}{Z}\right)\left(\frac{k_B T_\delta}{2}\right)$$

where δ is the phonon anomaly (in cm^{-1}), n is the degrees of freedom per atom, N is the number of atoms per unit cell, Z is the number of formula units per unit cell, k_B is Boltzmann's constant, and $k_B T_\delta/2$ is the well-known relationship between thermal energy and degrees of freedom [23].

The method to determine T_δ is outlined in previous work [23] and, for the $Mg_{1-x}Al_xB_2$ series, the value closely conforms with experimentally determined values of T_c. For Sc substitution, while there is greater variability in PDs with k-grid value, we adopt a similar approach to determine an average T_δ using the compiled values calculated from LDA and GGA models. This consistent approach to determine an average δ value allows assignment of confidence levels to estimates of T_δ in the transition from Mg–only to metal–substituted compositions.

Table 2 lists parameters determined by *ab initio* DFT calculations for other metal-substituted compositions using the same computational methods [23] to measure the presence or absence of a phonon anomaly in PD plots. These metal-substituted compositions include known compounds such as $Mg_{1-x}Ti_xB_2$ as well as $Mg_{1-x}Cd_xB_2$ and $Mg_{1-x}Ba_xB_2$ [23]. The searchable literature does not record experimental data on these latter two compounds. They

Table 1
Calculated Parameters for DFT models of $Mg_{1-x}Sc_xB_2$.

Structure	x	Optimized Unit Cell Parameters (Å)		DFT type	k-grid value	δ		Av. δ^a (cm^{-1})	Av. T_δ^a (K)
		a	c			(cm^{-1})	(meV)		
MgB_2	0.00	3.0391	3.4866	LDA	0.02	127.0	15.7	131.4 (6.2)	42.0 (2.0)
		3.0796	3.5538	GGA	0.02	135.8	16.8		
Mg_7ScB_{16}	0.125	3.0481	27.9457	LDA	0.032	109.7	13.6	116.2 (9.8)	37.1 (3.1)
		3.0860	28.4279	GGA	0.032	122.7	15.2		
Mg_6ScB_{14}	0.143	3.0520	24.3965	LDA	0.03	103.0	12.8	98.6 (13.9)	31.5 (4.4)
		3.0858	24.9029	GGA	0.027	94.1	11.7		
Mg_5ScB_{12}	0.167	3.0522	20.9534	LDA	0.016	113.9	14.9	112.0 (10.7)	35.8 (3.4)
		3.0875	21.3332	GGA	0.028	110.1	13.7		
Mg_4ScB_{10}	0.200	3.0550	17.4565	LDA	0.016	95.8	11.9	103.2 (9.6)	33.0 (3.1)
		3.0917	17.7411	GGA	0.027	110.6	13.7		
Mg_3ScB_8	0.250	3.0584	13.9792	LDA	0.017	36.2	4.5	35.5 (3.1)	11.4 (1.0)
		3.0924	14.2013	GGA	0.017	34.8	4.3		
Mg_2ScB_6	0.333	3.0660	10.4817	LDA	0.017	33.6	4.2	31.9 (3.6)	10.2 (1.2)
		3.0994	10.6322	GGA	0.017	30.3	3.8		
$MgScB_4$	0.500	3.0793	6.9848	LDA	0.017	36.4	4.5	27.6 (11.4)	8.8 (3.7)
		3.1097	7.0651	GGA	0.018	18.9	2.3		
$MgSc_2B_6$	0.667	3.0902	10.4772	LDA	0.021	21.0	2.6	23.0 (4.5)	7.4 (1.4)
		3.1176	10.5709	GGA	0.024	25.0	3.1		

[a] Standard deviation in parentheses.

remain to be synthesized provided the substituted metal is soluble in MgB_2.

4. Discussion

We have used *ab initio* DFT to estimate the decrease of T_c with increased substitution in $Mg_{1-x}Al_xB_2$ by measuring the thermal energy, T_δ, of an associated phonon anomaly [23]. This computational approach does not invoke *post facto* modification of band structure calculations nor new approximations or functionals to match theory with experiment [47,48]. The extent, or depth, of the anomaly associated with the dominant E_{2g} phonons is related to their thermal energy for excitation to higher B_{2g} modes and, for $Mg_{1-x}Al_xB_2$ compositions, matches within calculated error the experimental values of T_c [23]. The evidence to date suggests that structures which do not show a phonon anomaly may not be superconductors (e.g. AlB_2). That is, a phonon anomaly may be a necessary, but not sufficient, indicator of superconductivity for the AlB_2–type structure. To understand this link between materials theory and experiment, we consider other metal substituted forms of MgB_2 for which there are experimental data.

The $Mg_{1-x}Sc_xB_2$ system shows key differences to Al-substituted MgB_2 not only in the type and nature of valence electron orbitals but also in physical properties. For example, there is a two phase region, or solubility gap, at $0.07 < x < 0.13$ in $Mg_{1-x}Sc_xB_2$ [8] and again for $x > 0.27$ [10]. In addition, the experimentally determined superconducting T_c shows unusual behaviour at low doping levels of Sc [11] and approaches 6 K for $x \sim 0.27$ [8,49]. In comparison, Al is soluble in MgB_2 over a wide range of substitutions [50] with experimental evidence for superlattices [36]. Agrestini et al. also measure [9] the frequency, ω, of the E_{2g} Raman mode for $x < 0.3$ in $Mg_{1-x}Sc_xB_2$. The average value measured for ω is ~ 725 cm^{-1} which is consistent with the broad range of values calculated over all reciprocal lattice directions using *ab initio* DFT.

The $Mg_{1-x}Sc_xB_2$ and $Mg_{1-x}Ti_xB_2$ systems show higher complexity in both band structure and PD models compared with Al-substituted MgB_2 due to the influence of d orbital electrons and the associated metal-boron bonding. However, the fundamental attribute of the method we describe in this work, that is, to detect the presence or absence of a phonon anomaly around the recipro-

cal lattice origin, is demonstrable for $Mg_{1-x}Sc_xB_2$ as shown in Fig. 6 for $x = 0.17$ and $x = 0.20$. The partial PD for ScB_2 shown in Fig. 5c also indicates a small anomaly of the E_{2g} modes in the **G-K** and **G-M** directions. Experimental data indicates that ScB_2 is a superconductor at low temperature with T_c at 1.5 K [32].

4.1. Metal atom modelling

Superlattice structures along the c-axis are effective constructs that explain detailed experimental spectroscopy data for MgB_2 [18] and are also evident using electron microscopy for $Mg_{0.5}Al_{0.5}B_2$ [37] and other Al–substituted compositions [17,36]. For $Mg_{1-x}Sc_xB_2$ or $Mg_{1-x}Ti_xB_2$, similar observations of superlattice(s) are not evident in the literature. However, we have calculated the relative enthalpies for specific compositions of the Mg–Sc series to evaluate ordering preference. We calculate parameters for two different superlattice ordering models for $x = 0.33$ in the $Mg_{1-x}Sc_xB_2$ series. In contrast to calculations for $Mg_{1-x}Al_xB_2$, our evaluation of the Mg–Sc system shows that enthalpy favors a double stacking of Sc layers in an ordered motif. In this case, the difference in enthalpy between alternating layers and a double motif is ~ 0.02 eV. In comparison, the difference in enthalpy for $x = 0.33$ in $Mg_{1-x}Al_xB_2$ with the same stacking motif is ~ 0.14 eV.

The format of PD plots for a double stacking motif for Sc is similar to that for a single stacking motif but with a doubling of phonon modes consistent with the superlattice construct. However, there is a difference in the order of mode assignments when using LDA or GGA functionals. For doubly ordered motifs at $x = 0.33$ with $k = 0.02$ Å^{-1}, phonon anomalies are of greater magnitude compared with alternating layers of Mg and Sc. For this level of Sc substitution, the net effect is a higher level of uncertainty for the determination of T_δ. For comparison with the $Mg_{1-x}Al_xB_2$ series [23], we evaluate phonon anomalies in the Mg–Sc series by assuming alternate stacking of Mg and Sc layers along the c-axis direction.

4.2. Phonon dispersion modes

Point group symmetry evaluation of the AlB_2-type structure [13] shows that the E_{2u} and E_{2g} phonon modes are characterized
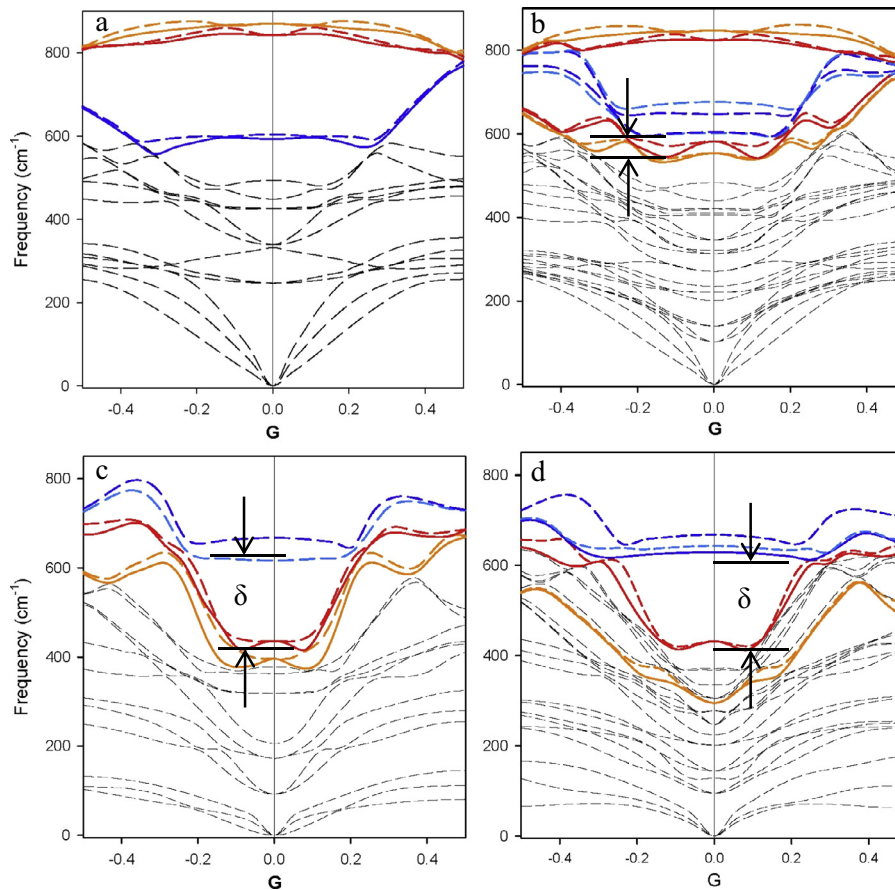
Fig. 7. Partial PD plots along **G-K** and **G-M** calculated using the GGA functional for (a) $MgTiB_4$, (b) Mg_3TiB_8, (c) $MgCdB_4$ and (d) Mg_2BaB_6. For these calculations k = 0.016 Å^{-1} except Fig. 7d for which k = 0.02 Å^{-1}. E_{2g} phonon modes are highlighted in red, E_{2u} modes are orange, B_{2g} modes are dark blue and B_{1u} modes are light blue. Note the extent of the phonon anomaly, δ, for $MgCdB_4$ and Mg_2BaB_6. (For interpretation of the references to color in this figure legend, the reader is referred to the web version of this article.)

Table 2
Calculated Parameters for DFT models of $Mg_{1-x}Ti_xB_2$ and $Mg_{1-x}Cd_xB_2$.

Structure	x	Optimized unit cell parameters		DFT type	k-grid value	Modelled DFT parameters δ		Av. δ[a]	Av. T_δ[A]
		a (Å)	c (Å)		(Å^{-1})	(cm^{-1})	(meV)	(cm^{-1})	(K)
Mg_3TiB_8	0.25	3.0574	13.9913	GGA	0.016	79.8	9.9	79.8 (10.0)	25.5 (3.2)
Mg_2TiB_6	0.33	3.0517	10.4265	GGA	0.016	55.6	6.9	55.6 (2.1)	17.8 (0.7)
$MgTiB_4$	0.50	3.0003	6.7242	LDA	0.020	20.1	2.5	15.3 (9.3)	4.9 (3.0)
		3.0417	6.8459	GGA	0.016	10.5	1.5		
Mg_2CdB_6	0.33	3.0672	10.7772	LDA	0.020	199.6	24.7	207.7 (10.5)	66.4 (3.4)
		3.1100	11.0319	GGA	0.022	215.9	26.8		
$MgCdB_4$	0.50	3.0811	7.2920	LDA	0.020	195.2	24.2	205.8 (14.4)	65.8 (4.6)
		3.1241	7.4802	GGA	0.022	216.3	26.8		
$MgCd_2B_6$	0.66	3.0896	11.1563	LDA	0.020	183.1	22.7	182.7 (6.0)	58.4 (1.9)
		3.1376	11.4232	GGA	0.022	182.3	22.6		

[a] Standard deviation in parentheses.

by a similar pattern of B atom movement within the a–b plane. The E_{2g} mode corresponds to the reciprocal space origin, **G**, and the E_{2u} mode corresponds to the **A** boundary along the c-axis direction. This correspondence introduces a phase shift in the vibrational motions of these atoms (with displacements having alternating signs at adjacent boron planes for E_{2g} modes at **A** for MgB_2 [13]). The relative energies of the E_{2g} and the E_{2u} modes will vary depending on the shape and orientation of the bonding orbitals interacting in the a–b plane.

In the $Mg_{1-x}Al_xB_2$ system, metal orbitals are p type and all lobes have alternating signs for electron density at opposite sides across the atom center (i.e. p orbitals do not have inversion symmetry

with respect to the metal). For bonding states, two overlapping lobes of the same sign will have a lower energy than antibonding states, where adjacent lobes have opposite sign. For MgB_2, theoretical and experimental evidence [51–53] suggest that p_σ and p_π orbitals are involved in bonding within the a–b plane. In this case, the bonding orbitals are combinations of Cartesian p orbitals with favorable sign overlap. The p orbital character in Mg and Al planes adjusts to the alternating signs of p orbitals in B planes to produce an overall favorable overlap and reduced energy.

However, in the $Mg_{1-x}Sc_xB_2$ system, each lobe of the Sc d orbitals shows the same sign with inversion symmetry at the Sc atom center. If these d orbitals are involved in bonding with p orbitals of

boron atoms, they will impose a different sign pattern surrounding the p orbitals of the boron planes. This situation is not favorable for maximum overlap of multiple layers. This requirement may break the inversion symmetry of the d orbitals across multiple layers and hence, will induce an opposite sign for the d orbital compared to the next nearest Sc layer.

The number of intercalated Mg and B planes between consecutive Sc planes, will determine whether overall inversion symmetry is manifest within a single superlattice or a double superlattice. The inversion symmetry (or loss of one) is a key difference between E_{2g} and E_{2u} modes, which are otherwise associated with the same pattern of atomic movement. Thus, the E_{2g} and E_{2u} modes in $Mg_{1-x}Sc_xB_2$ appear to be interchangeable vibration modes for this AlB_2–type structure. In certain cases, such as the partial PDs for Mg_5ScB_{12} and Mg_4ScB_{10} (Fig. 6) and $MgCdB_4$ (Fig. 7c), the E_{2u} mode closely follows the E_{2g} mode in form and extent.

4.3. Estimates of T_δ

Our estimate(s) of the phonon anomaly thermal energy within the AlB_2–type structure for a range of compositions, is at this stage, dependent on facile comparison with experimental data determined by a range of techniques. An important caveat for evaluation of $Mg_{1-x}M_xB_2$ is the method used to experimentally determine the value of x. The three substituted forms – $Mg_{1-x}Al_xB_2$, $Mg_{1-x}Mn_xB_2$ and $Mg(B_{1-x}C_x)_2$ – that are considered reliable and reproducible [3–5] are the result of multiple investigations with particular emphasis on elemental analysis determined after synthesis. Cava et al. [3] show that some early reports on metal substitutions in MgB_2 failed to meet this important criterion by assuming that product compositions matched the ratio of starting materials in synthesis. In this work, we compare our calculations with experimental determinations of composition for metal substituted MgB_2 after synthesis.

4.3.1. $Mg_{1-x}Sc_xB_2$

Fig. 8 shows the calculated average temperature T_δ (open red diamonds), associated with the phonon anomaly compared with experimentally determined T_c (solid symbols) as a function of Sc content in $Mg_{1-x}Sc_xB_2$. Experimental data for Fig. 8 are from the studies by Agrestini et al. [8,9]. The estimated errors for the calculated T_δ are obtained by combining data from models using the LDA and GGA functionals. The data in Fig. 8 and compiled in Table 1 also infers that compositions for x = 0.33 and x = 0.5 may be superconducting at low temperatures. To date, experimental data for these compositions are not available [8] and, implicitly, are insoluble levels of Sc substitution [9].

The *ab initio* prediction of T_δ for $Mg_{1-x}Al_xB_2$ is consistent with experimental values determined by resistivity or by magnetic measurements of the Meissner effect using values for the onset of superconductivity [23]. In contrast, the experimental determination of T_c for $Mg_{1-x}Sc_xB_2$ compositions [8,9,49] is obtained from peak values of surface resistance measurements. These peak determinations utilize the derivative of the change in surface resistance with temperature. For transitions with a substantial width and tail, this method will bias the estimate of T_c towards a lower temperature than the onset. For example, previous data [9] presented for surface resistance measurements on the composition x = 0.2 (i.e. $Mg_{0.8}Sc_{0.2}B_2$), clearly show that the onset takes place at about 22–23 K while a value from the peak determination is ∼15 K [9] (see also similar results for the $Mg_{1-x}Al_xB_2$ system [54]). The values for T_δ shown in Fig. 8 based on measurement of the magnitude of the anomaly are higher than that reported from experimental measurements [8]. However, if the difference between peak value of surface resistance and onset T_c is considered, the predicted values for T_δ obtained for this composition and for other
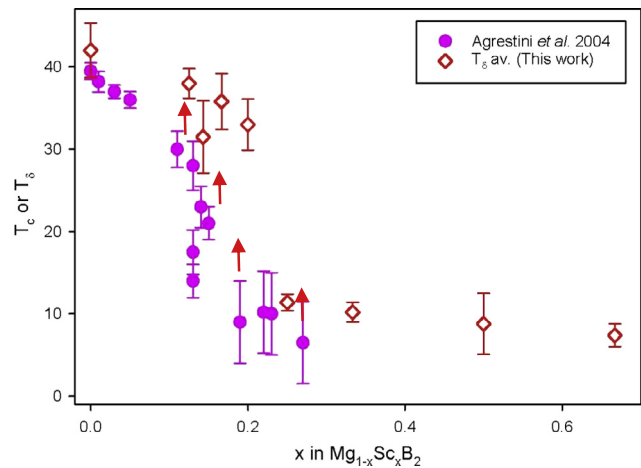
Fig. 8. Plot of experimental T_c values for $Mg_{1-x}Sc_xB_2$ (filled symbols) and calculated T_δ values (open symbols) determined by the *ab initio* method described in the text. The average T_δ values (red diamonds) are compilations of estimates from both LDA and GGA functional models. Error bars (this work) represent one standard deviation and are as reported by Agrestini et al. [9] Red arrows indicate the likely experimental values for onset T_c for this compositional series (see text for detail). (For interpretation of the references to color in this figure legend, the reader is referred to the web version of this article.)

Sc-substituted MgB_2 compositions match closely or are within the estimated errors.

Calculations using the LDA functional achieves convergence at lower k-grid values for x = 0.20 and x = 0.17 in $Mg_{1-x}Sc_xB_2$ as listed in Table 1. For these compositions, calculation with the GGA functional achieves convergence at a higher k-grid value (∼0.027 Å^{-1}). As noted earlier [18,23], the PD mode shape and order may be variable at these less dense grid intervals. Models that converge at different values of k-grid or at higher k-grid value (e.g. k = 0.03 Å^{-1}) contribute to larger error values for some estimates of T_δ shown in Fig. 8. For the other calculated compositions, k-grid values are similar or equal for both LDA and GGA functional models.

4.3.2. $Mg_{1-x}Ti_xB_2$

There are limited experimental data on T_c values for Ti substituted MgB_2 for which incorporation of Ti into the MgB_2 structure is confirmed. Zhao et al. [55] show that solid state synthesis of MgB_2 with Ti at ambient pressure results in concentration of Ti at the grain boundaries of MgB_2. However, high pressure experiments show that Ti is incorporated into the bulk matrix and that only minor Ti-rich phases occur in MgB_2 when synthesized at 2 GPa and 800 °C or 900 °C for 1 h [56]. We infer from their work that the MgB_2-Ti samples show a sharp transition and that for x = 0.1, the T_c ∼ 30 K [56]. Lee et al. have shown that Ti is uniformly doped into MgB_2 when synthesized at a higher pressure of 3 GPa and 1000 °C for 2 h [12]. Using transport and bulk sensitivity measurements with varying applied magnetic field, sharp transitions to superconductivity were observed in these samples [12]. In addition, magnetic susceptibility data indicate that the volume fraction of superconducting material is large in high pressure synthesized $Mg_{1-x}Ti_xB_2$ [12].

Magnetic susceptibility data for $Mg_{1-x}Ti_xB_2$ synthesized by Lee et al. [12] show a decrease in the onset T_c for Ti substitutions at x = 0.1, x = 0.2 and x = 0.4 [12]. From Fig. 2 in their work [12], we estimate the onset T_c for these Ti substitutions at 35 K, 30 K and 26 K, respectively. By measuring the extent of a phonon anomaly calculated using the *ab initio* DFT method described above, we also show that T_δ for Ti-substituted MgB_2 decreases as x increases. For example, at x = 0.25, x = 0.33 and x = 0.5, the calculated T_δ values are 25.5 (3.2) K, 17.8 (0.7) K and 4.9 (3.0) K, respectively (Table 2).

Note that Table 2 shows estimates of T_δ using both LDA and GGA functions for x = 0.5 only. For other compositions in this suite, convergence of LDA calculations was not achieved for the k-grid values evaluated (i.e. k ⩾ 0.016 Å^{-1}). For x = 0.33, an LDA calculation with k = 0.015 Å^{-1} gave an E_{2g} mode form and mode order that is inconsistent with the GGA results shown in Table 2 and Fig. 7. In general, we believe optimized models for $Mg_{1-x}Ti_xB_2$ require k-grid values ~0.01 Å^{-1} which demand computational capacity beyond current capability or require significant improvements in efficiency and speed of currently available codes.

4.3.3. Predicted compositions

We have calculated, by the same methodology, the estimated T_δ values for two other versions of metal-substituted MgB_2 that do not show a decrease in T_δ with substitution. These two compositional suites are $Mg_{1-x}Ba_xB_2$ and $Mg_{1-x}Cd_xB_2$. Compounds of either metal-substituted MgB_2 are not known nor experimentally verified at this time.

In earlier work [23], we show that DFT calculations on Ba-substituted MgB_2 indicate a strong E_{2g} phonon anomaly for 0.33 < x < 0.66. An example of this anomaly for x = 0.33 in $Mg_{1-x}Ba_xB_2$ is shown in Fig. 7d for which the estimated T_δ value is 64.4 (2.2) K. Similar estimated T_δ values in excess of 60 K are obtained for x = 0.5 and x = 0.66 [23]. These explicit diboride compositions are not yet known and may, indeed, not be possible to realize as the relative solubility of Ba in MgB_2 is unknown. Experimental and computed phase diagrams [57,58] for the intermetallic $BaMg_2$ and other compositions such as Ba_6Mg_{23} and Ba_2Mg_{17} suggests that these compounds are stable and will form at moderate temperatures (i.e. 350 °C to 600 °C). Thus, it may be possible to synthesize a series of Ba-substituted MgB_2 phases to validate the reliability of the methodology described in this work.

Ab initio DFT calculations for $Mg_{1-x}Cd_xB_2$ show small negative values for one mode at acoustic phonon frequencies on the **G-A** direction for x = 0.33 and x = 0.66. In both cases, the calculation converges at k = 0.02 Å^{-1} for the LDA functional and at k = 0.022 Å^{-1} for the GGA functional. These minor departures from a stable configuration suggest that Cd-substitution at these values is not ideal or that a lower k-grid value (i.e. k < 0.02 Å^{-1}) may be required to completely describe phonon behaviour. This latter point is evidenced by the full PD for $MgCdB_4$ (data not shown) in which all phonon frequencies are positive when calculated with k = 0.016 Å^{-1}. The partial PD for $MgCdB_4$ shown in Fig. 7c exemplifies the nature of the calculated phonon anomaly around the **G** reciprocal space point for x = 0.33 and x = 0.66. As with other phonon anomalies, the value of δ is measured for all branches of the E_{2g} modes in both the **G-M** and **G-K** directions calculated using the LDA and the GGA functionals [23]. This approach provides a robust estimate of the error for T_δ as shown in Table 2.

Table 2 shows the estimated average T_δ for $Mg_{1-x}Cd_xB_2$ where x = 0.33, 0.5 and 0.66. In each case, the calculated E_{2g} phonon anomaly shows similar magnitude to that for $Mg_{1-x}Ba_xB_2$ [23]. Thus, the T_δ values range from ~58 K to ~66 K across this compositional range using the E_{2g} modes to estimate δ. The estimated T_δ for $MgCdB_4$ is 65.8 (4.6) K. For x = 0.5, E_{2u} modes parallel the E_{2g} mode directions (Fig. 7c) with deeper extent of anomaly. If we assume that the E_{2g} and E_{2u} modes have similar effect and influence on superconductivity in metal-substituted MgB_2, estimates of δ using the E_{2u} modes suggest that the value of T_δ for $Mg_{0.5}Cd_{0.5}B_2$ could be as high as 76.9 (2.2) K. Again, these explicit diboride compositions are not yet known albeit the intermetallics Cd_3Mg, $CdMg$ and $CdMg_3$ are stable and form at relatively low temperatures (i.e. 150–250 °C) [59]. Nevertheless, computational convergence without negative phonon frequencies for $Mg_{0.5}Cd_{0.5}B_2$ indicates that this may be a stable phase if formed. Our experience with calculations for this structure type suggests that negative

phonon frequencies may be moderated or eliminated by simulating an applied pressure to the model structure [23].

Table 3 lists selected stoichiometric compositions for which we have calculated PDs using *ab initio* DFT. Estimates of T_δ, the thermal energy of the phonon anomaly around **G**, are compared with the experimentally observed T_c for each composition. The concordance of values between T_δ and T_c is remarkable given the estimated relative errors inherent in computational [66] and experimental [8,9,62] determinations. For each phase listed in Table 3, the presence of a phonon anomaly and the extent of the anomaly is consistent with the experimental determination of superconductivity.

4.4. Models and bonding orbitals

A well-known approach to predict, or to explain *post-facto*, experimentally determined T_c values involves estimates based on simplified solutions of the Eliashberg equations for T_c by using the McMillan formula [48] with assumptions on the value of the Coulomb pseudopotential, μ^*, and on the effective electron-phonon coupling constant, λ. The McMillan approximation has been used to estimate T_c for MgB_2 [13,47] but few reports evaluate metal substituted MgB_2. Neaton and Perali [67] used the McMillan approximation for Al-substituted MgB_2 to show a calculated T_c trend that follows experimental values but for a limited range of substitution (i.e. 0 < x < 0.08). We plot the average of these values determined by Neaton and Perali [67] in Fig. 9. A modification to DFT, termed superconducting DFT (SCDFT) [68,69] also matches the calculated superconducting gaps for MgB_2 with experimental data. SCDFT using a specific functional termed Random Phase Approximation (RPA) gave an estimate of T_c within 2 K of the experimental value [70] for MgB_2. Along similar lines for AlB_2-type structures, the application of McMillan equations to symmetry-related [18] "buckled" structures such as unsubstituted, end-member di-silicides (e.g. $RbSi_2$) and di-germanides (e.g. $RbGe_2$) as well as intercalated graphene (e.g. SrC_2) shows that upper limits to the value of T_c can be estimated for these structures [71]. In earlier work [23], we note the utility of the PD method outlined in this paper for estimation of T_δ for $BaSi_2$ and $Ca(Si_{0.5}Al_{0.5})_2$ which closely matches experimentally determined values [65,72] of T_c.

An *ab initio* VCA method demonstrated the evolution of σ and π bonding with increased substitution of Al in MgB_2 [35]. In this model, substitution of Al results in charge transfer from the Al–B bond such that an increased fraction of the charge is transferred to the π bond with an accompanying decreased fraction in σ bonds in the boron planes. This bonding shift results in a small but significant decrease in the distance between atomic planes along *c* with increase in Al composition. Using band structure calculations, de la Penha et al. [35] estimate a normalized hole density on the FS of $Mg_{1-x}Al_xB_2$ for 0 < x < 0.6 that correlates well with experimentally determined normalized superconducting T_c (i.e. T_c/T_0). A more complex approach by Kortus [47] used Eliashberg functions for MgB_2 combined with a VCA approximation for Al substitution to calculate the change in DOS at the FS, then re-calculated the band structure to solve the scaled Eliashberg functions to obtain a good correlation of calculated T_c with experimental measurements for 0 < x < 0.4.

We show the estimated T_c values for selected compositions calculated *via* the McMillan equation using the method described by Zheng and Zhu [73] in Table 4. This method estimates deformation potentials using the approach described by An and Pickett [74] which allows – for reasonable estimates of λ and μ^* – a comparison with values calculated by others [73,74] and, using our calculated DOS, an estimate of error for these values of T_c. This method uses strain-free MgB_2 as the geometry optimized reference structure to compare the DOS. The primary sources of error in this approach

Table 3
Calculated T_δ compared to experimental T_c for compositions of the AlB_2–type structure.

Composition	Estimated T_δ (K)	Reference	Experimental T_c (K)	References
MgB_2	42.0 (3.3)	[23]	39.2–40.2	[2,60,61]
$Mg_{0.8}Al_{0.2}B_2$	31.3 (3.4)	[23]	25 (2)–33.0 (0.1)	[50,62]
$Mg_{0.75}Al_{0.25}B_2$	26.1 (2.7)	[23]	19.0	[4]
$Mg_{0.67}Al_{0.33}B_2$	16.2 (3.3)	[23]	18.0 (2.0)	[62]
$Mg_{0.5}Al_{0.5}B_2$	4.6 (2.5)	[23]	4.0–13.5	[17,37,62]
$Mg_{0.33}Al_{0.67}B_2$	0.5 (0.3)	[23]	0.0 (0.1)	[50]
AlB_2	0.0	[23]	0.0	[45]
ScB_2	<5.0	This study	1.5	[32]
$Mg_{0.86}Sc_{0.14}B_2$	31.5 (4.4)	This study	23.0 (2.5)	[8,9]
$Mg_{0.75}Sc_{0.25}B_2$	11.4 (1.0)	This study	8.2 (5.0)	[8,9]
TiB_2	0.0	This study	0.0	[46,63]
$Mg_{0.75}Ti_{0.25}B_2$	25.5 (3.2)	This study	30	[12]; x = 0.2
$Mg_{0.67}Ti_{0.33}B_2$	17.8 (0.7)	This study	26	[12]; x = 0.4
$Mg_{0.5}Ba_{0.5}B_2$	63.6 (6.6)	[23]	na	–
$Mg_{0.5}Cd_{0.5}B_2$	65.8 (4.6)	This study	na	–
$BaSi_2$	9.3 (0.5)	[23]	8.9	[64]
$(Ca_{0.5}Al_{0.5})Si_2$	7.5 (0.5)	[23]	7.8	[64]
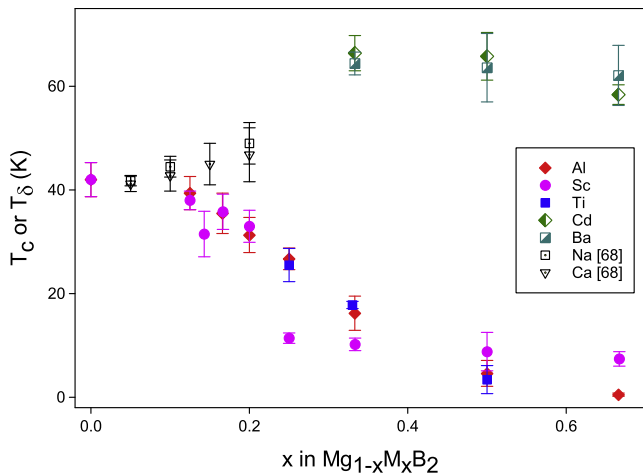
Fig. 9. Plot of calculated T_δ values for metal substituted MgB_2 determined by the *ab initio* DFT method described in the text except for Na- and Ca-substituted MgB_2 which are derived from the McMillan approximation to the Eliashberg equation [67]. T_δ values described in the text are averages derived from measurement of the phonon anomaly using both LDA and GGA functional models for each composition. Error bars represent one standard deviation.

rely upon the calculated DOS for the σ bands which, for MgB_2 and metal substituted forms, are tubular and warped towards the **G** point [75]. Values for the DOS of the σ bands are averaged with consideration for variation of the p orbital DOS close to the cusp (annotated in Fig. 3) and the different steep slopes of the σ band structures for the heavy and light effective masses. We elaborate on this approach under "McMillan Model" in Supplemental Material.

Table 4 shows that the agreement between the two approaches to estimate T_c – using a range of values for λ and μ^* or alternatively,

using measured values of δ from LDA and GGA PD plots – is reasonable within estimated errors. We include in Table 4 data calculated for MgB_2 under $-2GPa$ strain calculated by Zheng and Zhu [73] which conforms with experiments by Pogrebnyakov et al. [76] in which the strain-induced $T_c = 41.8$ K. The relative errors for T_c determined by the measurement of δ are lower than that calculated using the McMillan formalism due predominantly to the steep slope of the σ bands in the respective band structures. In addition, measurement of the phonon anomaly as shown in this work appears to reflect both electronic and phonon contributions and their interactions.

More recently, d'Astuto et al. [20] deployed the VCA model to compare with very high resolution IXS data on the E_{2g} phonon mode(s) at the zone centre (i.e. near and at **G** along the **G-M** and **G-A** directions) for MgB_2 and $Mg_{0.6}Al_{0.4}B_2$. The model for both compositions closely follows experimental data particularly in the regions at low reciprocal lattice dimension close to **G** (see right hand panel of Fig. 3 in d'Astuto et al. [20]; equivalent to the range 0–0.2 on the abscissa shown in Figs. 3–6 of this work). In this study [20], the close match between theory and experiment arises from inclusion of nonadiabatic effects in calculation of the E_{2g} PD. Thus, the experimental and computational steep rise in the PD near **G** (along **G-M**; and, we infer, also along **G-K**) is not an artefact [20]. This steep rise of the PD, for example in *ab initio* DFT models shown in Figs. 3, 4a, 6a and 7d, and also shown by experiment, is related to anomalous effects of the electron-phonon coupling near **G** or the zone centre [20].

The approach used in this work measures the extent of the phonon anomaly, in units of energy or frequency, as it is expressed by the calculated E_{2g} vibration modes evident in a PD plot. We determine the average thermal energy, T_δ, of this anomaly along the two important bonding orientations in the AlB_2 type structure based on *ab initio* DFT calculations using two functionals that use different algorithms to describe electron density distribution [21,66]. In Fig. 9, we plot metal substituted MgB_2 compositions and their

Table 4
Comparison of calculated T_c by McMillan formalism with phonon anomaly method (this work).

	T_c (K) MgB_2 at -2 GPa			T_c (K) Mg_5ScB_{12}			T_c (K) $MgCdB_4$		
λ	$\mu^* = 0.15$	$\mu^* = 0.10$	$\mu^* = 0.15$[73]	$\mu^* = 0.15$	$\mu^* = 0.10$	δ	$\mu^* = 0.15$	$\mu^* = 0.10$	δ
0.94	42.8(4.6)	42.0(3.6)	41.8(0.8)[a]	29.9(7.6)	31.6(6.1)	35.8(3.4)	60.2(11.5)	54.5(9.1)	65.8(4.6)
0.80	43.9(5.8)	42.7(4.5)	–	27.6(9.7)	30.1(7.5)		67.6(14.6)	59.5(11.2)	

[a] Estimated from Fig. 4 of Zheng and Zhu[73].

estimated T_δ determined via *ab initio* DFT calculations using LDA and GGA functionals as described in this work. We also show in Fig. 9 calculated T_c values determined by Neaton and Perali [67] using the McMillan approximation to Eliashberg equations [48] for Na- and Ca-substituted MgB$_2$. Neaton and Perali [67] used this approach to show that a small decrease in electron density can increase the DOS at the Fermi level and can also increase T_c. We re-plot their values for T_c shown in their Figs. 6 and 7 [68] for $\mu^* = 0.1$ and for the Gruneisen parameter, $\gamma = 1.0$ in Mg$_{1-x}$Na$_x$B$_2$ and Mg$_{1-x}$Ca$_x$B$_2$ for $0 < x < 0.2$. In Fig. 9, we estimate errors for these values by taking the standard deviation of T_c determined for $\gamma = 0$ and $\gamma = 2.0$ due to greater influence of the Gruneisen parameter on these calculated T_c values [67].

Fig. 9 reveals two general trends as noted earlier for this structure type [67]. In one case, the T_δ decreases with substitution of Al, Sc or Ti (filled symbols) while in the other the T_δ increases with substitution of Ba and Cd and the calculated T_c increases as predicted for Na and Ca [67] (partial and unfilled symbols). For the metal ions Mg^{+2}, Ca^{+2}, Ba^{+2} and Cd^{+2}, the valence configuration involves fully occupied s orbitals and predominantly s–p bonding as shown for MgB$_2$ [52,62]. Na$^+$ has an unoccupied s orbital and will also invoke s–p bonding when substituted into MgB$_2$ [67], solubility permitting. In comparison, Al^{+3}, Sc^{+3} and Ti^{+4} bonding with boron in this type structure will involve unoccupied d or p valence orbitals. Divalent substitutions show predominantly s–p bonding while trivalent or tetravalent substitutions will involve d–p or p–p bonding orbitals. With increased concentration of a substituent trivalent or tetravalent ion in MgB$_2$, increased transfer of electrons to π bonding orbitals is consistent with a reduction of cell dimensions along the c axis [35,67] and a reduction in cell volume. Conversely, substitution of Na, Ca, Cd and Ba increases the cell volume and likely reduces transfer of electrons to π bonding orbitals in preference to σ bonding.

Fig. 10 shows the optimized unit cell volume for metal substituted MgB$_2$ calculated in this study using LDA and GGA functionals. For superlattice structures in this series, the c axis value is adjusted to account for the multiplicity of the basic lattice unit. With the exception of Sc-substituted MgB$_2$, cell volume varies with composition along similar trends as shown in Fig. 10 for T_δ. Compared to the case for Al and Ti, the calculated cell volumes for Mg$_{1-x}$Sc$_x$B$_2$ show a small increase ($\sim$3.5% on average) with increasing value of x. Table 1 shows that the a axis dimensions for Sc substitution calculated by both functionals increase by $\sim$2% relative to MgB$_2$ with increased x. This cell dimension trend, particularly for the a axis, is consistent with experimental data obtained for partially

substituted Mg$_{1-x}$Sc$_x$B$_2$ for $0.13 < x < 0.27$ [8,9]. The increase in the calculated c axis dimension (Table 1) is $\sim$1% relative to MgB$_2$ in contrast to a reduction in c axis value with Al and Ti substitution at $\sim$5% and $\sim$10%, respectively. The increase in cell volume for Sc substitution is minimal compared with Cd or Ba substitution at $\sim$11% and $\sim$35%, respectively, for x = 0.66. Thus, the change in c axis dimension for Sc substituted MgB$_2$ is small in comparison to other calculated substitutions.

The models for increased DOS [67] and for the change in hole density [35] at the FS for metal substituted MgB$_2$ are implicitly attributed to a significant and consistent change in the c axis dimension which influences the bonding environment for both σ and π orbitals. However, the calculated and experimental data for Mg$_{1-x}$Sc$_x$B$_2$ show that the a axis measurably increases while the c axis dimension is relatively unchanged. This change in dimension implies a different influence on the electronic structure at the FS compared with other models [35,67]. A reduction in the strength, or extent, of the phonon anomaly is clear from PD plots (see Figs. 5 and 6 and Table 1) and is noted by Agrestini et al. [9]. Charge density in the boron layers predominantly influences the position of the Fermi level relative to the σ bands. We suggest that for the solubility levels of Sc substitution in MgB$_2$, the Fermi level shifts relative to the σ bands due to the influence of d orbitals and a resultant change in the DOS at the FS.

The method described in this work provides a capacity to explicitly design other metal diboride configurations that allow a potentially higher T_δ value than that currently identified. For example, substitution of Hg, Zn, or Sr may be interesting compositions to pursue if these elements are soluble in MgB$_2$. Our calculations and interpretation for this diboride structure implicitly supports the notion that key aspects of superconductivity including the electron–phonon interaction is well modelled by quasiparticle behaviour in PD plots calculated via *ab initio* DFT methods.

5. Conclusions

For the AlB$_2$–type structure, the orientation and frequency of the E$_{2g}$ phonons is critical to superconductivity. A phonon anomaly is observed experimentally and *via* model calculations in MgB$_2$ and metal substituted MgB$_2$. Calculated values for the thermal energy of the phonon anomaly using *ab initio* DFT closely resemble experimentally determined values of T_c for MgB$_2$ with substantive substitutions of Sc and Ti. This match of the calculated phonon anomaly thermal energy with experimental data is consistent with similar analysis of Al substituted MgB$_2$. In addition, this *ab initio* DFT method to measure δ provides estimates of T_c for known and predicted metal substituted MgB$_2$ compositions that are similar to estimates determined by the deformation potential variation of the McMillan formalism. We extend calculation of the E$_{2g}$ phonon anomaly thermal energy to other, as yet not synthesized metal substituted MgB$_2$, such as Mg$_{0.5}$Cd$_{0.5}$B$_2$ and Mg$_{0.67}$Ba$_{0.33}$B$_2$. From this, we predict values of T_δ for these compositions are 65.8 (4.6) K and 64.4 (2.2) K, respectively, and propose that the value of T_c for these putative compositions will be of similar order. Model outcomes for these phonon anomalies are systematically consistent for compositional suites of metal substituted MgB$_2$ and for other compositions within the AlB$_2$–type structure.
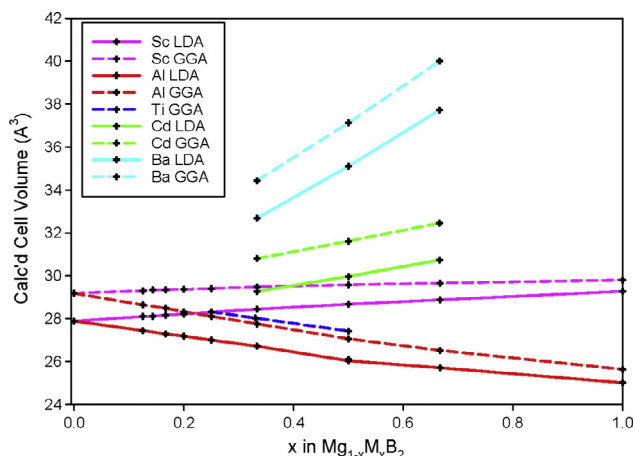
Fig. 10. Calculated cell volumes determined from optimized unit cell parameters using *ab initio* DFT models with LDA or GGA functionals for metal substituted compositions of MgB$_2$. Data points obtained from models used in this study are denoted by "+".

Appendix A. Supplementary material

Supplementary data associated with this article can be found, in the online version, at http://dx.doi.org/10.1016/j.commatsci.2017.01.011.

References

[1] C. Buzea, T. Yamashita, Topical review – review of the superconducting properties of MgB$_2$, Supercond. Sci. Technol. 14 (2001) R115.
[2] J. Nagamatsu, N. Nakagawa, T. Muranaka, Y. Zenitani, J. Akimitsu, Superconductivity at 39 K in magnesium diboride, Nature 410 (2001) 63.
[3] R.J. Cava, H.W. Zandbergen, K. Inumaru, The substitutional chemistry of MgB$_2$, Physica C 385 (2003) 8.
[4] J. Karpinski, N.D. Zhigadlo, S. Katrych, R. Puzniak, K. Rogacki, R. Gonnelli, Single crystals of MgB$_2$: synthesis, substitutions and properties, Physica C 456 (2007) 3.
[5] J. Karpinski, N.D. Zhigadlo, S. Katrych, K. Rogacki, B. Batlogg, M. Tortello, R. Puzniak, MgB$_2$ single crystals substituted with Li and Li-C: structural and superconducting properties, Phys. Rev. B 77 (2008), 214507.
[6] S.L. Bud'ko, P.C. Canfield, Superconductivity of magnesium diboride, arXiv: 1501.06948v1 2015.
[7] S. Lee, H. Mori, T. Masui, Y. Eltsev, A. Yamamoto, S. Tajima, Growth, structure analysis and anisotropic superconducting properties of MgB$_2$ single crystals, J. Phys. Soc. Jpn. 70 (8) (2001) 2255.
[8] S. Agrestini, C. Metallo, M. Filippi, G. Campi, C. Sanipoli, S. De Negri, M. Giovannini, A. Saccone, A. Latini, A. Bianconi, Sc doping of MgB$_2$: the structural and electronic properties of Mg$_{1-x}$Sc$_x$B$_2$, J. Phys. Chem. Solids 65 (8–9) (2004) 1479.
[9] S. Agrestini, C. Metallo, M. Filippi, L. Simonelli, G. Campi, C. Sanipoli, E. Liarokapis, S. De Negri, M. Giovannini, A. Saccone, et al., Substitution of Sc for Mg in MgB$_2$: effects on transition temperature and Kohn anomaly, Phys. Rev. B 70 (13) (2004) 134514.
[10] M. Filippi, S. Agrestini, L. Simonelli, N.L. Saini, A. Bianconi, S. De Negri, M. Giovannini, A. Saccone, X-ray absorption near edge structure (XANES) microscopy of phase separation in superconducting Mg$_{1-x}$Sc$_x$B$_2$, Spectrochim. Acta Part B – Atomic Spectrosc. 62 (6–7) (2007) 717.
[11] M. Filippi, L. Simonelli, S. Agrestini, M. Fratini, V. Palmisano, G. Campi, C. Sanipoli, S. De Negri, M. Giovannini, A. Saccone, et al., T$_c$ as a function of electron doping in (MgB$_2$)-B^{10} using Sc for Mg substitution, J. Supercond. 18 (5–6) (2005) 667.
[12] B.W. Lee, I. Choia, C.U. Junga, S.I. Leeb, Doping in MgB$_2$ superconductors using a high-pressure furnace, J. Magn. Magn. Mater. 320 (2008) e484.
[13] K. Kunc, I. Loa, K. Syassen, R.K. Kremer, K. Ahn, MgB$_2$ under pressure: phonon calculations, Raman spectroscopy, and optical reflectance, J. Phys.: Condens. Matter 13 (2001) 9945.
[14] A.Q.R. Baron, H. Uchiyama, Y. Tanaka, S. Tsutsui, D. Ishikawa, S. Lee, R. Heid, K.-P. Bohnen, S. Tajima, T. Ishikawa, Kohn anomaly in MgB$_2$ by inelastic X-Ray scattering, Phys. Rev. Lett. 92 (2004) 197004.
[15] J. Kortus, I.I. Mazin, K.D. Belashchenko, V.P. Antropov, L.L. Boyer, Superconductivity of metallic boron in MgB$_2$, Phys. Rev. Lett. 86 (20) (2001) 4656.
[16] R. Heid, K.-P. Bohnen, B. Renker, Electron-phonon coupling and superconductivity in MgB$_2$ and related diborides, Adv. Solid State Phys. 42 (2002) 293.
[17] J.Y. Xiang, D.N. Zheng, J.Q. Li, L. Li, L.P.L. Lang, H. Chen, C. Dong, G.C. Che, Z.A. Ren, H.H. Qi, et al., Superconducting properties and c-axis superstructure of Mg$_{1-x}$Al$_x$B$_2$, Phys. Rev. B 65 (2002) 214536.
[18] J.A. Alarco, A. Chou, P.C. Talbot, I.D.R. Mackinnon, Phonon modes of MgB$_2$: super-lattice structures and spectral response, Phys. Chem. Chem. Phys. 16 (2014) 24443.
[19] A.Q.R. Baron, H. Uchiyama, S. Tsutsui, Y. Tanaka, D. Ishikawa, J.P. Sutter, S. Lee, S. Tajima, R. Heid, K.-P. Bohnen, Review: phonon spectra in pure and carbon doped MgB$_2$ by inelastic X-ray scattering, Physica C 456 (2007) 83.
[20] M. d'Astuto, R. Heid, B. Renker, F. Weber, H. Schober, O. De la Pena-Seaman, J. Karpinski, N.D. Zhigadlo, A. Bossak, M. Krisch, Nonadiabatic effects in the phonon dispersion of Mg$_{1-x}$Al$_x$B$_2$, Phys. Rev. B 93 (180508R) (2016) 1.
[21] S. Baroni, S. De Gironcoli, A. Dal Corso, P. Giannozzi, Phonons and related crystal properties from density-functional perturbation theory, Rev. Mod. Phys. 73 (2) (2001) 515.
[22] F. Giustino, Materials Modelling Using Density Functional Theory – Properties and Predictions, Oxford University Press, 2014.
[23] J.A. Alarco, P.C. Talbot, I.D.R. Mackinnon, Phonon anomalies predict superconducting T$_c$ for AlB$_2$-type structures, Phys. Chem. Chem. Phys. 17 (2015) 25090.
[24] K. Refson, S.J. Clark, P.R. Tulip, Variational density functional perturbation theory for dielectrics and lattice dynamics, Phys. Rev. B 73 (2006) 155114.
[25] S.J. Clark, M.D. Segall, C.J. Pickard, P.J. Hasnip, M.I.J. Probert, K. Refson, M.C. Payne, First principles methods using CASTEP, Z. Kristallogr. 220 (2005) 567.
[26] J.A. Alarco, P.C. Talbot, I.D.R. Mackinnon, Coherent phonon decay and the boron isotope effect for MgB$_2$, Phys. Chem. Chem. Phys. 16 (2014) 25386.
[27] V.I. Anisimov, F. Aryasetiawan, A.I. Lichtenstein, First-principles calculations of the electronic structure and spectra of strongly correlated systems: the LDA + U method, J. Phys.: Condens. Matter 9 (1997) 767.
[28] B. Himmetoglu, A. Floris, S. de Gironcoli, M. Cococcioni, Hubbard-corrected DFT energy functionals: the LDA+U description of correlated systems, Int. J. Quantum Chem. 114 (1) (2014) 14.
[29] K.-P. Bohnen, R. Heid, B. Renker, Phonon dispersion and electron-phonon coupling in MgB$_2$ and AlB$_2$, Phys. Rev. Lett. 86 (25) (2001) 5771.
[30] A. Waskowska, L. Gerward, J.S. Olsen, K.R. Babu, G. Vaitheeswaran, V. Kanchana, A. Svane, V.B. Filipov, G. Levchenko, A. Lyaschenko, Thermoelastic properties of ScB$_2$, TiB$_2$, YB$_4$ and HoB$_4$: experimental and theoretical studies, Acta Mater. 59 (2011) 4886.
[31] S. Agrestini, C. Metallo, M. Filippi, L. Simonelli, G. Campi, C. Sanipoli, E. Liarokapis, S. De Negri, M. Giovannini, A. Saccone, Substitution of Sc for Mg in MgB$_2$: effects on transition temperature and Kohn anomaly, Phys. Rev. B 70 (13) (2004) 134514.
[32] S.M. Sichar, V.M. Antonov, Electronic structure, phonon spectra and electron–phonon interaction in ScB$_2$, Low Temp. Phys. 39 (7) (2013) 595.
[33] K. Momma, F. Izumi, VESTA 3 for three-dimensional visualization of crystal, volumetric and morphology data, J. Appl. Crystallogr. 44 (6) (2011) 1272.
[34] Accelrys, 2016.
[35] O. de la Penha, A. Aguayo, R. de Coss, Effects of Al doping on the structural and electronic properties of Mg$_{1-x}$Al$_x$B$_2$, Phys. Rev. B 66 (2002) 01251.
[36] H.W. Zandbergen, M.Y. Wu, H. Jiang, M.A. Hayward, M.K. Haas, R.J. Cava, The complex superstructure in Mg$_{1-x}$Al$_x$B$_2$ at x~0.5, Physica C 366 (2002) 221.
[37] J.Q. Li, L. Li, F.M. Liu, C. Dong, J.Y. Xiang, Z.X. Zhao, Superconductivity, superstructure, and structure anomalies in Mg$_{1-x}$Al$_x$B$_2$, Phys. Rev. B 65 (2002) 132505.
[38] S.F. Matar, Electronic structure and chemical bonding within MgB$_2$ and related borides from first principles, Z. Naturforsch. 63b (2008) 673.
[39] I. Loa, K. Kunc, K. Syassen, P. Bouvier, Crystal structure and lattice dynamics of AlB$_2$ under pressure and implications for MgB$_2$, Phys. Rev. B 66 (13) (2002) 134101.
[40] D.R. Armstrong, The electronic structure of the first-row transition metal diborides, Theoret. Chim. Acta 64 (1983) 137.
[41] R. Kumar, M.C. Mishra, B.K. Sharma, V. Sharma, J.E. Lowther, V. Vyas, G. Sharma, Electronic structure and elastic properties of TiB$_2$ and ZrB$_2$, Comput. Mater. Sci. 61 (2012) 150.
[42] S.M. Sichkar, V.N. Antonov, V.P. Antropov, Comparative study of the electronic structure, phonon spectra and electron-phonon interaction of ZrB$_2$ and TiB$_2$, Phys. Rev. B 87 (064305) (2013) 1.
[43] Y. Han, Y. Dai, D. Shu, J. Wang, B. Sun, Electronic and bonding properties of TiB$_2$, J. Alloys Compd. 438 (2007) 327.
[44] T. Morshedloo, M.R. Roknabadi, M. Behdani, First-principles study of the superconductivity in MgB$_2$ bulk and in its bilayer thin film based on electron–phonon coupling, Physica C 509 (2015) 1.
[45] V.P.S. Awana, A. Vajpayee, M. Mudgel, H. Kishan, Superconductivity of various borides and the role of carbon in their high performance, Supercond. Sci. Technol. 22 (2009) 034015.
[46] R. Heid, B. Renker, H. Schober, P. Adelmann, D. Ernst, K.P. Bohnen, Lattice dynamics and electron-phonon coupling in transition metal diborides, Phys. Rev. B 67 (2003) 180510.
[47] J. Kortus, Current progress in the theoretical understanding of MgB$_2$, Physica C 456 (2007) 54.
[48] A.Y. Liu, I.I. Mazin, J. Kortus, Beyond Eliashberg superconductivity in MgB$_2$: anharmonicity, two-phonon scattering, and multiple gaps, Phys. Rev. Lett. 87 (2001) 087005.
[49] S. Agrestini, C. Metallo, M. Filippi, G. Campi, C. Sanipoli, A. Saccone, S. De Negri, M. Giovannini, A. Latini, A. Bianconi, in: M. Stutzmann (Ed.), Physica Status Solidi C: Magnetic and Superconducting Materials, Proceedings, vol. 1, 2004.
[50] L.G. Sevastyanova, O.K. Gulish, V.A. Stupnikov, V.K. Genchel, O.V. Kravchenko, B.M. Bulychev, R.A. Lunin, V.P. Tarasov, Structure and properties of solid solutions in the Mg-Al-B system, Cent. Eur. J. Phys. 10 (1) (2012) 189.
[51] H.J. Choi, D. Roundy, H. Sun, M.L. Cohen, S.G. Louie, The origin of the anomalous superconducting properties of MgB$_2$, Nature 418 (2002) 758.
[52] I.I. Mazin, V.P. Antropov, Electronic structure, electron-phonon coupling, and multiband effects in MgB$_2$, Physica C 385 (2003) 49.
[53] P. Szabó, P. Samuely, J. Kačmarčík, T. Klein, J. Marcus, D. Fruchart, S. Miraglia, C. Marcenat, A. Jansen, Evidence for two superconducting energy gaps in MgB$_2$ by point-contact spectroscopy, Phys. Rev. Lett. 87 (13) (2001) 137005.
[54] A. Bianconi, S. Agrestini, D. Di Castro, G. Campi, G. Zangari, N.L. Saini, A. Saccone, S. De Negri, M. Giovannini, G. Profeta, et al., Scaling of the critical temperature with the Fermi temperature in diborides, Phys. Rev. B 65 (17) (2002) 174515.
[55] Y. Zhao, Y. Feng, C.H. Cheng, L. Zhou, Y. Wu, T. Machi, Y. Fudamoto, N. Koshizuka, M. Murakami, High critical current density of MgB$_2$ bulk

superconductor doped with Ti and sintered at ambient pressure, App. Phys. Lett. 79 (8) (2001) 1154.

[56] T.A. Prikhna, W. Gawalek, Ya.M. Savchuk, V.E. Moshchil, N.V. Sergienko, T. Habisreuther, M. Wendt, R. Hergt, Ch. Schmidt, J. Dellith, et al., High-pressure synthesis of MgB_2 with addition of Ti, Physica C 402 (2004) 223.

[57] W.W. Scott Jr., M.J. DeHaemer, in: H. Baker (Ed.), Alloy Phase Diagrams, vol. 3, ASM International, 1998.

[58] Y. Zhiwen, D. Jinglian, W. Bin, H. Chuanzheng, R. Melnik, First principles studies on the structural, elastic, electronic properties and heats of formation of Mg-AE (AE = Ca, Sr, Ba) intermetallics, Intermetallics 32 (2013) 156.

[59] Z. Moser, W. Gasior, J. Wypartowicz, L. Zabdyr, The Cd-Mg (cadmium-magnesium) system, Bull. Alloy Phase Diagrams 5 (1) (1984) 23.

[60] S. Bud'ko, G. Lapertot, C. Petrovic, C. Cunningham, N. Anderson, P. Canfield, Boron isotope effect in superconducting MgB_2, Phys. Rev. Lett. 86 (9) (2001) 1877.

[61] D. Hinks, H. Claus, J. Jorgensen, The complex nature of superconductivity in MgB_2 as revealed by the reduced total isotope effect, Nature 411 (6836) (2001) 457.

[62] M. Putti, M. Affronte, P. Manfrinetti, A. Palenzona, Effects of Al doping on the normal and superconducting properties of MgB_2: a specific heat study, Phys. Rev. B 68 (094514) (2003) 1.

[63] A.Q.R. Baron, H. Uchiyama, R. Heid, K.P. Bohnen, Y. Tanaka, S. Tsutsui, D. Ishikawa, S. Lee, S. Tajima, Two-phonon contributions to the inelastic x-ray scattering spectra of MgB_2, Phys. Rev. B 75 (2007) 020505.

[64] J.A. Flores-Livas, R. Debord, S. Botti, A. San Miguel, S. Pailhes, M.A.L. Marques, Superconductivity in layered binary silicides: a density functional theory study, Phys. Rev. B 84 (2011) 184503.

[65] M. Imai, K. Nishida, T. Kimura, H. Abe, Superconductivity of $Ca(Al_{0.5}, Si_{0.5})_2$, a ternary silicide with the AlB_2-type structure, Appl. Phys. Lett. 80 (6) (2002) 1019.

[66] L. He, F. Liu, G. Hautier, M.J.T. Oliveira, M.A.L. Marques, F.D. Vila, J.J. Rehr, G.-M. Rignanese, A. Zhou, Accuracy of generalized gradient approximation functionals for density-functional perturbation theory calculations, Phys. Rev. B 89 (2014) 064305.

[67] J.B. Neaton, A. Perali, in: arXiv:cond-mat/0104098 [cond-mat.supr-con]; Cornell University Library: http://arxiv.org/abs/cond-mat/0104098v1, 2001.

[68] N.N. Lathiotakis, M.A.L. Marques, M. Luders, L. Fast, E.K.U. Gross, Density functional theory for superconductors, Int. J. Quantum Chem. 99 (2004) 790.

[69] L.N. Oliveira, E.K.U. Gross, W. Kohn, Density-functional theory for superconductors, Phys. Rev. Lett. 60 (23) (1988) 2430.

[70] A. Floris, A. Sanna, M. Luders, G. Profeta, N.N. Lathiotakis, M.A.L. Marques, C. Franchini, E.K.U. Gross, A. Continenza, S. Massidda, Superconducting properties of MgB_2 from first principles, Physica C 456 (2007) 45.

[71] J.A. Flores-Livas, A. Sanna, Superconductivity in intercalated group-IV honeycomb structures, Phys. Rev. B 91 (2015) 054508.

[72] J.A. Flores-Livas, R. Debord, S. Botti, A. San Miguel, M.A.L. Marques, S. Pailhes, Enhancing the superconducting transition temperature of $BaSi_2$ by structural tuning, Phys. Rev. Lett. 106 (2011) 087002.

[73] J.-C. Zheng, Y. Zhu, Searching for a higher superconducting transition temperature in strained MgB_2, Phys. Rev. B 73 (2) (2006) 024509.

[74] J.M. An, W.E. Pickett, Superconductivity of MgB_2: Covalent bonds driven metallic, Phys. Rev. Lett. 86 (19) (2001) 4366.

[75] Y. Kong, O.V. Dolgov, O. Jepsen, O.K. Andersen, Electron-phonon interaction in the normal and superconducting states of MgB_2, Phys. Rev. B 64 (020501) (2001) 1.

[76] A.V. Pogrebnyakov, J.M. Redwing, S. Raghavan, V. Vaithyanathan, D.G. Schlom, S.Y. Xu, Q. Li, D.A. Tenne, A. Soukiassian, X.X. Xi, et al., Enhancement of the superconducting transition temperature of MgB_2 by a strain-induced bond-stretching mode softening, Phys. Rev. Lett. 93 (14) (2004) 147006.